ELSEVIER

Volume 181, Number 4, April 2008

JOURNAL OF SOLID STATE CHEMISTRY

www.elsevier.com/locate/jssc

CONTENTS

Abstracted/indexed in BioEngineering Abstracts, Chemical Abstracts, Coal Abstracts, Current Contents/Physics, Chemical, & Earth Sciences, Engineering Index, Research Alert, SCISEARCH, Science Abstracts, and Science Citation Index. Also covered in the abstract and citation database SCOPUS®. Full text available on ScienceDirect®.

Regular Articles

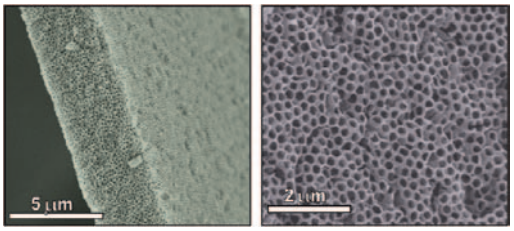

Thin films materials of mixed oxides with potential application in SOFC devices have been prepared with macroporous microstructure using PMMA microspheres as pore formers.

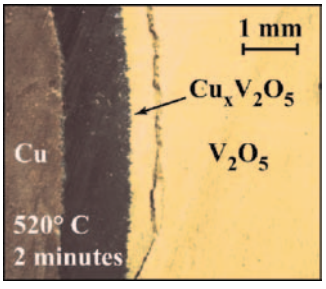

Fast diffusion of Cu into V_2O_5 is studied on Cu–V_2O_5 diffusion couples sintered by spark plasma sintering. The shape of the diffusion profiles is explained by the influence of phase transitions and by the concentration dependence of the diffusion coefficient. High value of diffusion coefficient is measured ($D \approx 3 \times 10^{-8}\,m^2/s$).

Regular Articles—Continued

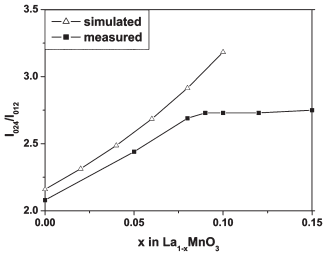

The X-ray diffraction intensity ratio of (024) and (012) reflections of $La_{1-x}MnO_{3\pm\delta}$ I_{024}/I_{012} increases with x until $x=0.09$ as predicted by the computer simulation, and at $x>0.09$ the intensity ratio levels off, showing that the maximum lanthanum deficiency is around 0.09.

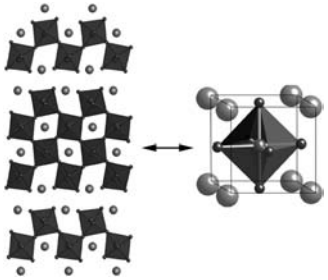

Phase selection of $SrNbO_y$ films is influenced primarily by the process gas (in the 1–100 mTorr pressure range). In oxygen, films adopt the $Sr_2Nb_2O_7$ (110)-layered perovskite structure (left). In nitrogen, films adopt the cubic perovskite $SrNbO_3$ structure (right). The films' microstructure depends, however, on the substrate type and temperature.

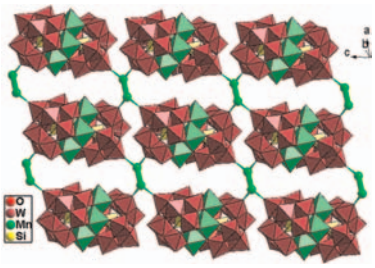

Five new compounds, from zero- to two-dimensional built up of the sandwich-type clusters and transition-metal linkers, have been obtained by the routine synthetic reactions in aqueous solution. This polyoxoanion framework architecture represents the first example of the 2D structure consisting of the sandwich-type polyoxoanion $[Mn_4(H_2O)_2(SiW_9O_{34})_2]^{12-}$ and the binuclear $\{Mn_2(H_2O)_6\}^{4+}$ group.

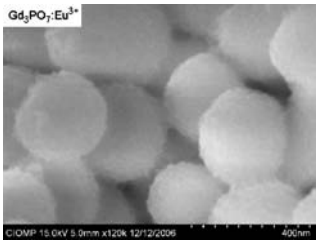

SEM image of as-prepared Gd_3PO_7:Eu^{3+} nanospheres.

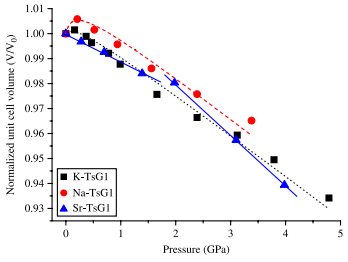

Three different cation forms of gallosilicate CGS zeolites have been investigated using synchrotron X-ray powder diffraction and a diamond-anvil cell. Under hydrostatic conditions, unit-cell lengths and volume show anomalous compression behaviours depending on the non-framework cation type and initial hydration level, which implies different modes of pressure-induced hydration and channel distortion.

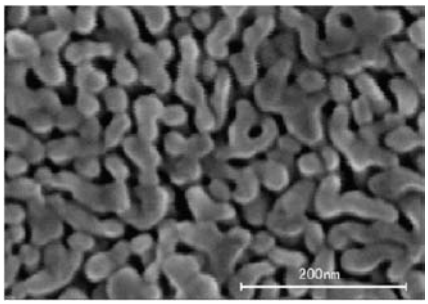

A novel and facile synthesis route for the manufacture of transparent and uniform nanocrystalline α-Fe_2O_3 (nc-Fe_2O_3) thin films or powders with wormlike morphology is reported, utilizing ferric nitrate as the inorganic source and triblock copolymer as the wormlike morphology–structure-directing agent through evaporation-induced assembly (EIA).

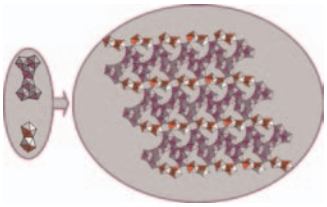

View of the $^2_\infty[U_8O_{36}]$ uranyl infinite layer formed by association of $[U_6O_{30}]$ and $[U_2O_{12}]$ uranyl blocks in $Cs_9[(UO_2)_8O_4(NbO_5)(Nb_2O_8)_2]$.

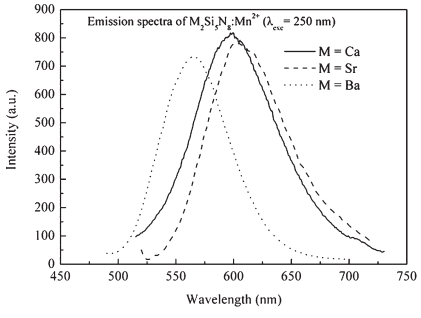

The luminescence properties of Mn^{2+} in $M_2Si_5N_8$ (M = Ca, Sr, Ba) have been investigated. All $M_2Si_5N_8$:Mn^{2+} phosphors show narrow symmetric bands in the wavelength range of 500–700 nm with peak center at about 599, 606 and 567 nm for M = Ca, Sr, Ba, respectively. The observed band emission is ascribed to the $^4T_1(^4G) \rightarrow {}^6A_1(^6S)$ transition of Mn^{2+} in $M_2Si_5N_8$ host lattice.

Continued

Synthesis of the titanium phosphide telluride Ti_2PTe_2: A thermochemical approach
Frauke Philipp, Peer Schmidt, Edgar Milke, Michael Binnewies and Stefan Hoffmann
page 758

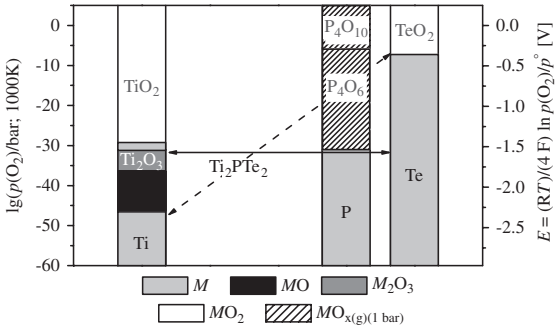

Oxygen partial pressure and electrochemical potential above the oxides of titanium, tellurium and phosphorus calculated at 1000 K, marked: level of equalisation of oxygen partial pressure.

Structure and electrical transport properties of the ordered skutterudites $MGe_{1.5}S_{1.5}$ (M = Co, Rh, Ir)
Paz Vaqueiro, Gerard G. Sobany and Martin Stindl
page 768

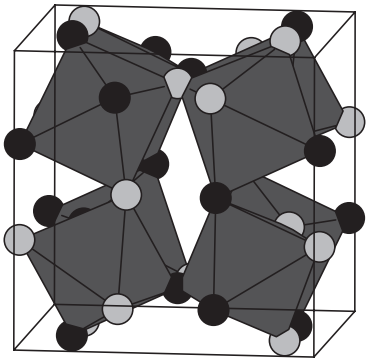

The $MGe_{1.5}S_{1.5}$ phases exhibit an ordered skutterudite structure, in which the anions form diamond-like four-membered Ge_2S_2 rings.

Structural aspects of fast copper mobility in Cu_6PS_5Cl—The best solid electrolyte from Cu_6PS_5X series
A. Gagor, A. Pietraszko and D. Kaynts
page 777

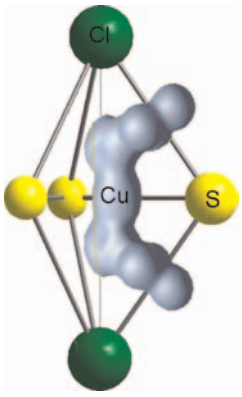

Coordination of copper mobile ions in superionic phase of Cu_6PS_5Cl, $T = 435$ K.

Solid-state synthesis in the system $Na_{0.8}Nb_yW_{1-y}O_3$ with $0 \leqslant y \leqslant 0.4$: A new phase, $Na_{0.5}NbO_{2.75}$, with perovskite-type structure
Tapas Debnath, Claus H. Rüscher, Thorsten M. Gesing, Jürgen Koepke and Altaf Hussain
page 783

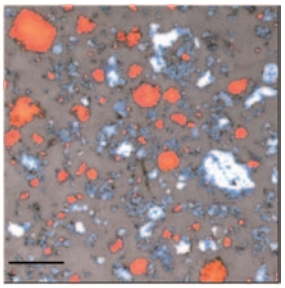

Optical micrograph of a polished sample of nominal composition $Na_{0.8}Nb_{0.4}W_{0.6}O_3$ showing a mixture of three different coloured crystals: red, light blue and white. The scale bar is 30 μm.

Linear and nonlinear optical susceptibilities for a novel borate oxide $BaBiBO_4$: Theory and experiment
Ali Hussain Reshak, S. Auluck and I.V. Kityk
page 789

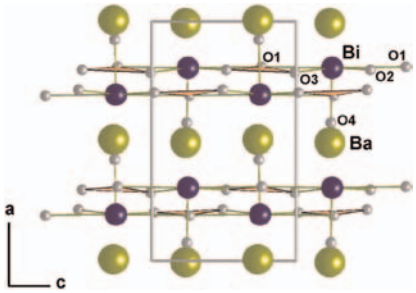

Principal crystalline structure.

A study of the phase transitions and proton dynamics of the superprotonic conductor $Cs_5H_3(SO_4)_4 \cdot 0.5H_2O$ single crystal with ^1H and ^{133}Cs nuclear magnetic resonance
Ae Ran Lim
page 796

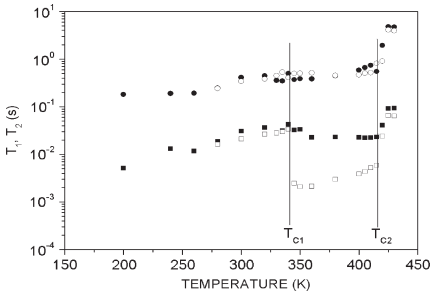

The phase transitions and proton dynamics of $Cs_5H_3(SO_4)_4 \cdot 0.5H_2O$ were studied by the spin-lattice relaxation time and the spin–spin relaxation time of the ^1H and ^{133}Cs nuclei. The "acid" and the "water" protons were distinguished. Our NMR study has provided new information about the roles of acid protons, water protons, and cesium nuclei in $Cs_5H_3(SO_4)_4 \cdot 0.5H_2O$ single crystals. Fig. Temperature dependences of T_1 and T_2 for acid and water protons in a $Cs_5H_3(SO_4)_4 \cdot H_2O$ single crystal (●: T_1 and ■: T_2 for acid proton, ○: T_1 and □: T_2 for water proton).

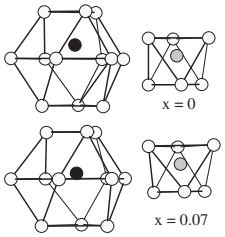

$Bi_{1-x}K_xFeO_3$ ($0 \leqslant x \leqslant 0.07$) are described in *R*3*c* space group. The average Fe (gray balls) and Bi/K (black balls) displacements decrease with K content reducing the polar character and leading to a change from rhombohedral to pseudo-cubic symmetry. Structural disorder results in strong diffuse scattering. The compounds remain antiferromagnetic at room temperature.

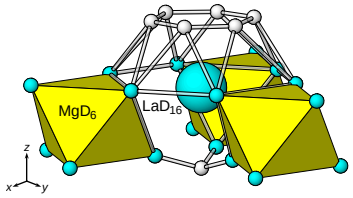

Substitution of La by Mg in La_2Ni_7 occurs only in the Laves-type parts of the crystal structure to form $LaMgNi_4$ slabs within the $La_{1.5}Mg_{0.5}Ni_7$ crystal. Subsequent hydrogenation forms $La_{1.5}Mg_{0.5}Ni_7D_{9.1}$ with a nearly isotropic expansion of the unit cell that is in contrast to the large unilateral anisotropic expansion that takes place on hydrogenation of La_2Ni_7. Contrary to $La_2Ni_7D_{6.5}$ where only $LaNi_2$ layers absorb hydrogen atoms leaving $LaNi_5$ slabs unmodified, in $La_{1.5}Mg_{0.5}Ni_7D_{9.1}$ both $LaNi_5$ and $LaMgNi_4$ layers become occupied; the effect of Mg substitution is the increase of the reversible hydrogenation storage capacity. Within the hydrogen sublattice inside the $LaMgNi_4D_{7.56}$ slab local ordering of Mg and La in the layer gives a packing of the MgD_6 octahedra and LaD_{16} polyhedra as shown.

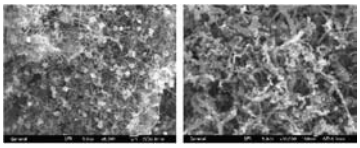

Multiwalled carbon nanotube (MWNT)/flower-like ZnO heterojunctions and MWNT/ZnO nanoparticle composites were prepared by zinc–ammonitum complex ion covalently attached to the MWNTs through the C–N bonds via adjusting the reaction time. A growth mechanism has been proposed in which the soaking time plays a key role in controlling the size, morphology, and site of ZnO nanostructures.

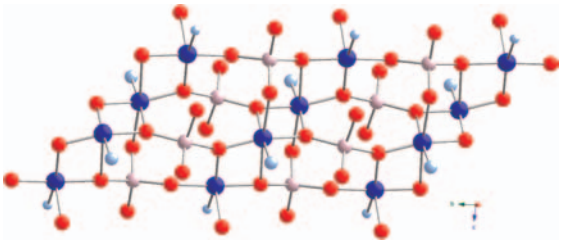

$[Cu_2(MoO_4)_2(3,4'\text{-dpk})(H_2O)]$ (**1**, 3,4′-dpk = 3,4′-dipyridylketone) and $[Cu_4(3,4'\text{-dpk})_4(Mo_8O_{26})]$ (**2**) have been prepared by hydrothermal methods. **1** possesses 1-D $[Cu_2(MoO_4)_2(H_2O)]_n$ ribbons containing magnetically interacting $\{Cu_4O_6\}$ tetramers. The ribbons are connected into 2-D by 3,4′-dpk ligands. The reduced phase **2** manifests an unprecedented 1-D "X-rail" chain motif.

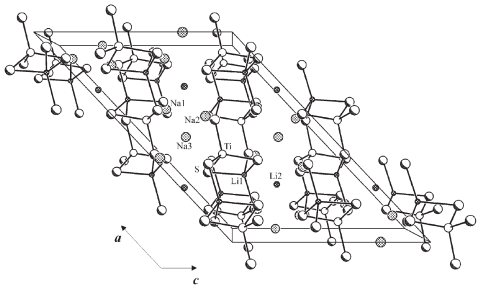

The structure of $Na_5Li_3Ti_2S_8$ viewed down [010]. For the sake of clarity, the Na–S and Li(2)–S interactions are omitted.

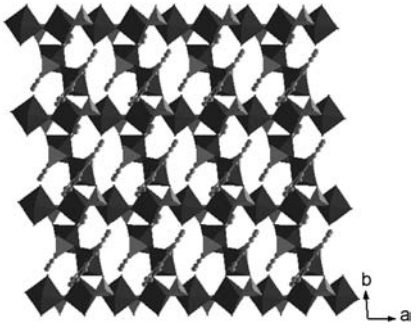

The two-dimensional layer structure of (2,2′-bipy)$[In_2(OH)_2(H_2O)](SO_4)_2$ along [001].

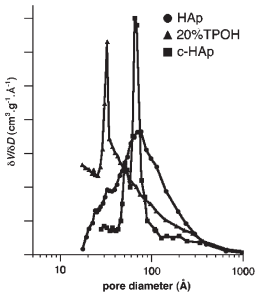

Evolution of pore size distribution of hydroxyapatite (HAp) after alkylphosphonate grafting (20% TPOH) or citrate addition c-HAp) demonstrates the formation of organically modified mesoporous materials.

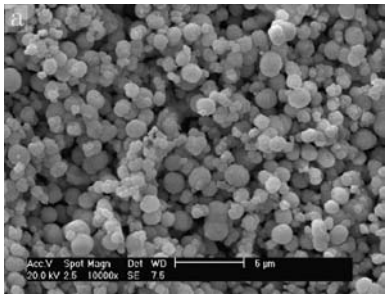

Submicro-crystalline Eu^{3+}-activated tungstate $CaWO_4$:RE^{3+} phosphors with a sheelite structure have been synthesized via the hydrothermal process; the morphology was determined from the hydrothermal temperature. Scanning electron microscopy (SEM) images show that $CaWO_4$:Eu^{3+} exhibits spherical particles, which can be controlled by the reaction parameters.

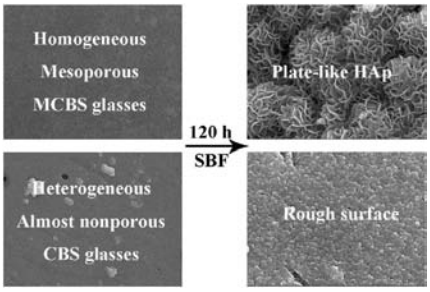

Surfactant-templated mesoporous CaO–B_2O_3–SiO_2 glasses (MCBS) are superior to conventional sol–gel-derived CaO–B_2O_3–SiO_2 glasses (CBS) in compositional homogeneity, textural properties and in vitro bioactivity.

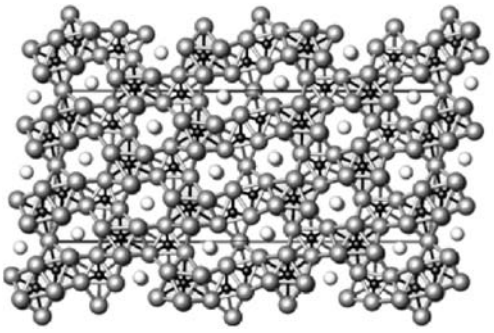

A 3D structure built of bi- and tricapped trigonal prisms centered by Ru or Te.

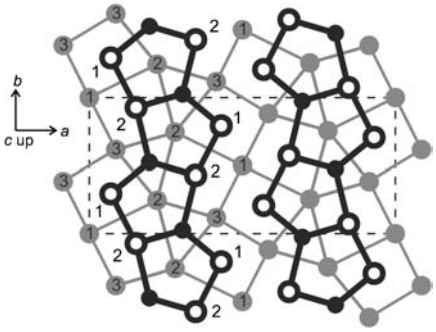

Crystal structure of $Dy_5Ni_2In_4$.

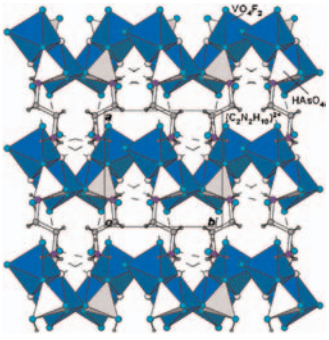

Polyhedral view of the layered crystal structure of $(C_2H_{10}N_2)_{0.5}$[(VO)($HAsO_4$)F].

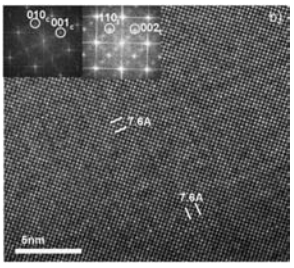

HRTEM image of a crystal of $Sr_{0.5}Ca_{0.5}CrO_3$ showing a random distribution of $2\mathbf{a}_p \approx 7.6$ Å all along the crystal that lacks long range order. Inset shows the FFT of the area of the image and of a tenth of that area showing the influence of the coherence length.

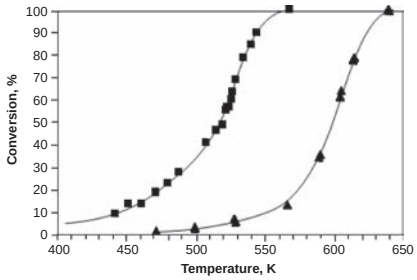

$LaFeO_3$, $LaNiO_3$ and substituted $LaFe_{1-y}Ni_yO_3$ ($y = 0.1$, 0.2 and 0.3) perovskite-type oxides have been investigated as catalysts in the total combustion of ethanol and acetylacetate. The characterization indicate variation in specific surface area, crystal structure, reducibility and surface composition. The catalytic activity expressed as intrinsic activity ($mol\,m^{-2}\,h^{-1}$) increases with nickel substitution. A synergy between Ni^{3+} and Fe^{3+} cations at the B position of the $LaFe_{1-y}Ni_yO_3$ perovskite for VOCs combustion was observed.

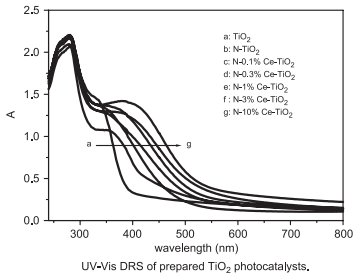

UV-Vis DRS of prepared TiO_2 photocatalysts.

A novel TiO_2 photocatalyst codoped with nitrogen and cerium was synthesized and characterized. An enhanced visible light activity was achieved. UV–vis DRS results indicated that the optical absorption edge of the N–Ce codoped TiO_2 was obviously shifted to the visible light range as the Ce/Ti doping ratio increased.

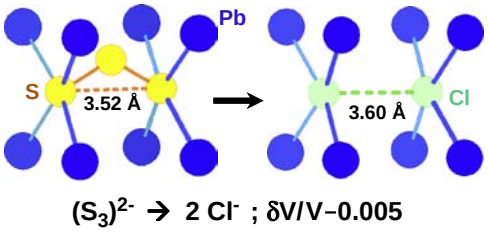

The title compound, $Pb_{3+x}Sb_{3-x}S_{7-x}Cl_{1+x}$, is derived from the homeotypic persulfide $Pb_6Sb_6S_{14}(S_3)$ by substituting two chlorine atoms for the S_3 trimer. This change is quite isovolumic.

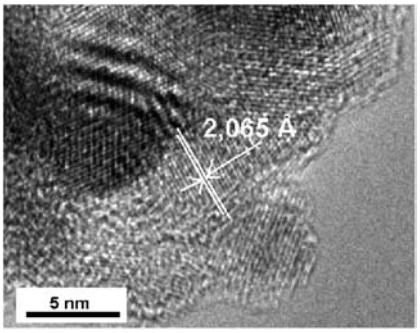

Nanocrystalline ternary V–Mo nitrides were prepared via nitridation of amine intercalated oxide foams or bulk ternary oxides. Foamed precursors were favorable for vanadium rich materials, while for molybdenum rich samples bulk ternary oxides resulted in higher specific surface areas.

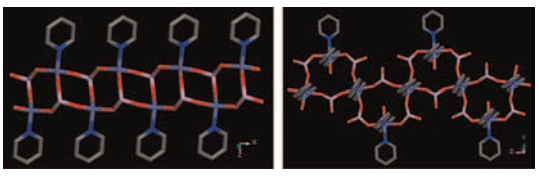

Two new 1D inorganic–organic hybrid cobalt (II) phosphites have been prepared under solvothermal conditions in the presence of pyridine. $Co(HPO_3)$ (py) possesses a 1D ladder-like framework constructed from CoO_3N tetrahedral, HPO_3 pseudo-pyramids and pyridine ligands (left); 1D-chain structure of $[Co(OH)(py)_3][Co(py)_2][HPO_2(OH)]_3$ consists of corner-shared six-membered rings (right).

Size-tunable synthesis of tetrapod-like ZnS nanopods by seed-epitaxial metal-organic chemical vapor deposition
Tianyou Zhai, Yang Dong, Yaobing Wang, Zongwei Cao, Ying Ma, Hongbing Fu and Jiannian Yao
page 950

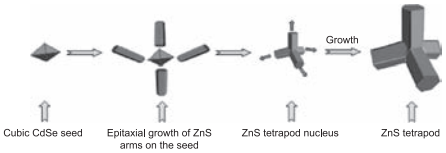

Single-crystalline tetrapod-like ZnS nanopods were synthesized by a one-step seed-epitaxial metal-organic chemical vapor deposition approach using cubic CdSe nanocrystals as the seeds. The diameters of the ZnS tetrapods can be easily tuned by changing the distances between the substrates and precursors.

Microwave-induced synthesis of highly dispersed gold nanoparticles within the pore channels of mesoporous silica
Jinlou Gu, Wei Fan, Atsushi Shimojima and Tatsuya Okubo
page 957

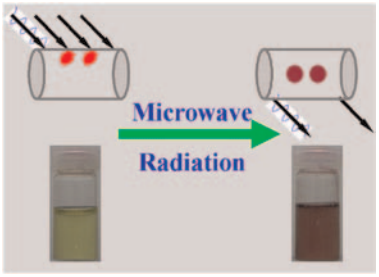

A facile and novel strategy has been developed to incorporate gold nanoparticles into the pore channels of mesoporous SBA-15 assisted by microwave radiation (MR) with mild reaction condition and rapid reaction speed. Due to the rapid and homogeneous nucleation, simultaneous propagation and termination by MR, the size of gold nanoparticles are effectively controlled.

Synthesis, crystal structure, and photocatalytic activity of a new two-layer Ruddlesden–Popper phase, $Li_2CaTa_2O_7$
Zhenhua Liang, Kaibin Tang, Qian Shao, Guocan Li, Suyuan Zeng and Huagui Zheng
page 964

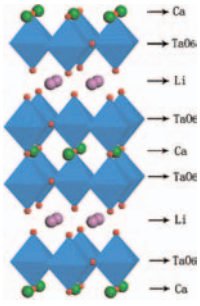

Crystal structure of a two-layer Ruddlesden–Popper phase $Li_2CaTa_2O_7$. A new two-layer Ruddlesden–Popper phase $Li_2CaTa_2O_7$ has been synthesized for the first time. $Li_2CaTa_2O_7$ crystallizes in the space group *Fmmm* determined by powder X-ray and electron diffraction. UV–visible diffuse reflection spectra and the photocatalytic degradation of RhB molecules in water under ultra visible light irradiation show that $Li_2CaTa_2O_7$ is a potential material in photocatalysis.

Twinned tetragonal structure and equation of state of $NaTh_2F_9$
Andrzej Grzechnik, Wolfgang Morgenroth and Karen Friese
page 971

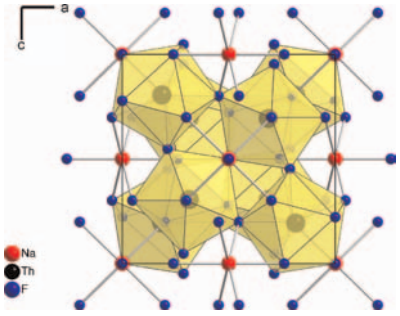

Crystal structure of $NaTh_2F_9$ ($I\bar{4}2m$, $Z=4$) at ambient conditions. The polyhedra around the Th atoms are drawn.

Topotactic insertion of lithium in the layered structure $Li_4VO(PO_4)_2$: The tunnel structure $Li_5VO(PO_4)_2$
M. Satya Kishore, V. Pralong, V. Caignaert, S. Malo, S. Hebert, U.V. Varadaraju and B. Raveau
page 976

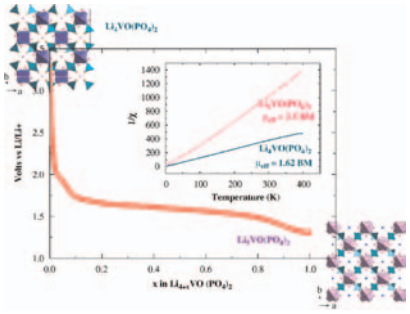

Electrochemical synthesis of a new 3D V(III) lithium phosphate, $Li_5VO(PO_4)_2$. Starting from the 2D $Li_4VO(PO_4)_2$, the topotactic reaction that take place during lithium intercalation is explained on the basis of the flexible coordinations of V^{4+} and V^{3+} species.

Atomistic simulation on the site preference and mechanical properties of $Th_3Co_{4+x}Al_{12-x}$ and $U_3Co_{4+x}Al_{12-x}$
Ping Qian, Hui-Jun Tian, Nan-Xian Chen and Jiang Shen
page 983

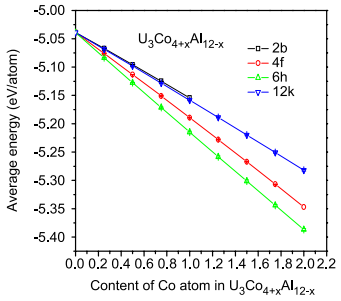

It is seen from figure that the substitution of Co for Al at all the four sites 2*b*, 4*f*, 6*h* and 12*k* decrease the cohesive energy of $U_3Co_{4+x}Al_{12-x}$, which means that the Co atoms can play a role in stabilizing the structure. The Co atoms strongly prefer 6*h* sites.

Continued

Author inquiries

Submissions

For detailed instructions on the preparation of electronic artwork, consult the journal home page at http://authors.elsevier.com.

Other inquiries

Visit the journal home page (http://authors.elsevier.com) for the facility to track accepted articles and set up e-mail alerts to inform you of when an article's status has changed. The journal home page also provides detailed artwork guidelines, copyright information, frequently asked questions and more.

Contact details for questions arising after acceptance of an article, especially those relating to proofs, are provided after registration of an article for publication.

Language Polishing

Authors who require information about language editing and copyediting services pre- and post-submission should visit http://www.elsevier.com/wps/find/authorshome.authors/languagepolishing or contact authorsupport@elsevier.com for more information. Please note Elsevier neither endorses nor takes responsibility for any products, goods, or services offered by outside vendors through our services or in any advertising. For more information please refer to our Terms & Conditions at http://www.elsevier.com/wps/find/termsconditions.cws_home/termsconditions.

For a full and complete Guide for Authors, please refer to *J. Solid State Chem.,* Vol. 180, Issue 1, pp. *bmi–bmv*. The instructions can also be found at http://www.elsevier.com/wps/find/journaldescription.cws_home/622898/authorinstructions.

Journal of Solid State Chemistry has no page charges.